Analyses of pre- and post-peak behavior of deep beams failed in shear using 3D-RBSM

Y.H. Gedik, H. Nakamura & M. Kunieda
Department of Civil Engineering, Nagoya University, Japan

Y. Yamamoto
Department of Civil & Environmental Engineering, National Defense Academy, Japan

ABSTRACT: The behaviors of deep beams failed in shear were investigated using 3D-RBSM, which is a representative method of discrete method that presents realistic behavior from cracking to the failure. Two deep beams without web reinforcement were analyzed having shear span ratio (a/d) of 0.5 and 1.5. Analytical results were compared with the experimental ones in terms of load displacement graph and crack pattern and it was confirmed that RBSM is a useful tool for the analysis. Moreover, the strut width and high stress state as well as deformation were investigated three dimensionally and 3D behavior of deep beams due to shear span ratio was discussed. As a result, failure behavior of deep beams failed in shear was clarified by discussing the three-dimensional behavior.

1 INTRODUCTION

The shear failure behavior of RC deep beams is complex task and it is affected by compression failure of concrete, shear cracking propagation, bond and anchorage of re-bar and so on. Thus, it is one of the difficult problems of numerical simulation in concrete structures. Finite Element Method (FEM), which is the major numerical tool of concrete structures, is based on continuum mechanics. However, the failure of concrete structures exhibits discontinuous behavior. Especially, the failure of deep beams localizes near support and loading points with the complex high stress state. When the localization behavior is simulated by FEM, unreasonable behavior is often observed such as instability problem because of inconsistency with continuum mechanics. On the other hand, numerical methods based on discrete mechanics have been proposed and applied to concrete structures. Rigid-Body-Spring Model (RBSM) is one of them and it is a representative method of discrete element method, which was firstly proposed by Kawai (Kawai 1978). It can show realistic behavior from cracking to failure. RBSM can also investigate stress transfer mechanism in meso levels (Yamamoto et al. 2008).

In this study, pre- and post-peak behaviors of RC deep beams in shear failure are investigated in detail using 3D-RBSM. The numerical analysis is applied on the experimental work of Kosa and others (Kosa et al. 2005, 2006). Two deep beams without web reinforcement in shear span are analyzed having shear span ratio (a/d) of 0.5 and 1.5. The load displacement graph, crack propagation and crack pattern obtained by RBSM analysis are compared with experimental results and the applicability is discussed.

Then, three-dimensional behavior such as lateral deformations is investigated by the analytical results. The strut widths and high stress state in deep beams are also investigated and the behavior on middle and surface longitudinal section is compared. Three-dimensional effect of deep beams failed in shear is discussed.

2 ANALYTICAL METHOD

2.1 *Three-dimensional RBSM*

Concrete is modeled as an assemblage of rigid particles interconnected by springs along their boundaries in 3D-RBSM. Continuum mechanics provides the internal behavior of each particle. However, the response of spring model assures insight of the interaction between the particles instead. Three translational and three rotational springs are defined at the nuclei of each rigid particle (Fig. 1.a). The boundary surface between two particles is divided into several triangles having the center of gravity and vertices of the surface shown in the figure. The integral point has one normal and two tangential springs. This model can consider the effect of bending and torsional moment spontaneously without setting any rotational springs (Yamamoto et al. 2008).

The cracks initiate and propagate through the interface boundaries between particles. Therefore, the mesh design of the structure strongly affects the crack pattern. Thus, Voronoi diagram is used in order to generate random network of rigid particles (Fig. 1.b) that reduces the mesh bias on potential crack initiation and propagation (Bolander et al. 2000)
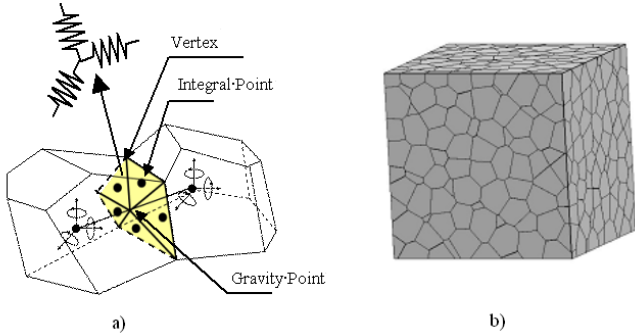

Figure 1. a) Rigid body spring model b) Voronoi Diagram.

Reinforcement is modeled by a series of beam elements that can be placed independently without depending the concrete discretization (Bolander et al. 2002). The nodes at beam-ends have two translational and one rotational degree of freedom. Linkage elements provide the connection between beam elements and concrete particles. Load transfer between beam nodes and concrete particles is provided by these linkage elements (Saito 1999).

2.2 Concrete model

Concrete material models are given in Figure 2. The tensile model of normal spring is shown in Figure 2.a. ¼ tensile model is employed. Tensile fracture energy is considered in the model.
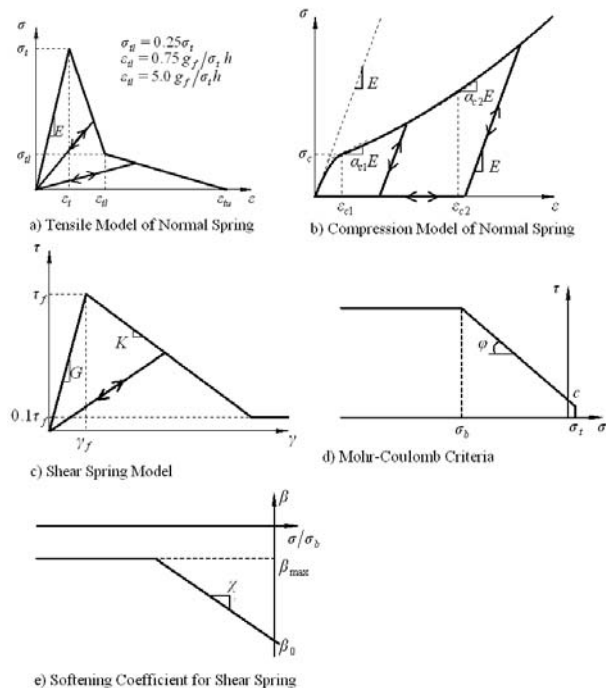

Figure 2. Material models (Yamamoto et al. 2008).

Figure 2.b shows the compression model of the normal spring. The model was developed by Yamamoto and others (Yamamoto et al. 2008). The model consists of two functions given in Equation 1. ε_{c1}, a_0, b_0, a_1, b_1 and c_1 are obtained by parametric analyses.

$$\sigma = \begin{cases} a_0 \varepsilon^2 + b_0 \varepsilon & (\varepsilon > \varepsilon_{c1}) \\ a_1 \varepsilon^2 + b_1 \varepsilon + c_1 & (\varepsilon \leq \varepsilon_{c1}) \end{cases} \quad (1)$$

Figure 2.c shows the shear spring model. Two tangential springs is combined in this model. Shear strain is given by equation 2 where the strains of each spring are γ_l and γ_m. The stress for each spring is obtained by Equation 3.

$$\gamma = \sqrt{\gamma_l^2 + \gamma_m^2} \quad (2)$$

$$\tau_l = \tau (\gamma_l/\gamma), \ \tau_m = \tau (\gamma_m/\gamma) \quad (3)$$

The stress increases elastically until the shear strength having the slope of shear modulus G. Mohr-Coulomb type criteria for shear is given in Figure 2.d. The slope of softening part (K) is given by equation 4 where β is obtained from the graph given in Figure 2.e and G is the shear modulus. In the model, the shear stress decreases by increase of crack width.

$$K = \beta G \quad (4)$$

In this model, compressive failure of normal spring does not occur. However, the model can simulate compressive failure behavior with confinement effect by the combination of normal spring and shear springs. Figure 3 shows the stress strain relationship obtained from the simulation of uniaxial compression test of the concrete for specimen B2 and B10, which are explained in the next chapter.
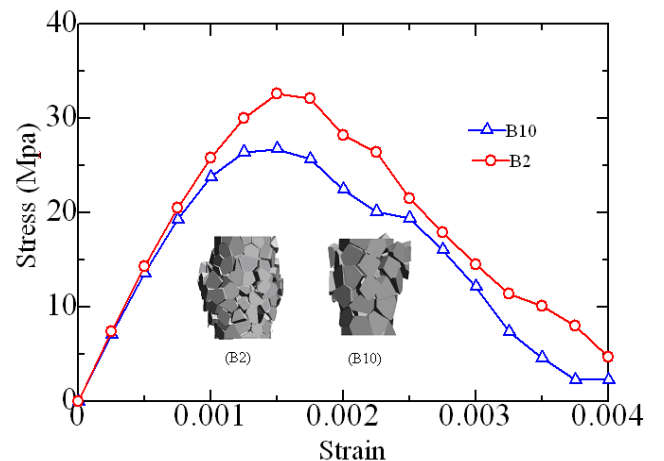

Figure 3. Stress-strain relationship and deformed shapes of uniaxial compression tests.

3 ANALYZED SPECIMENS

Analyses are performed for two deep beams, that is, B2 and B10 having no web reinforcement in shear span (Kosa et al. 2005 and 2006). The shear span ratios are 0.5 and 1.5 respectively (Table 1). Specimens' details are shown in Figure 4 and 5

Table 1. Overview of specimens.

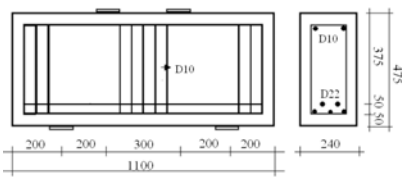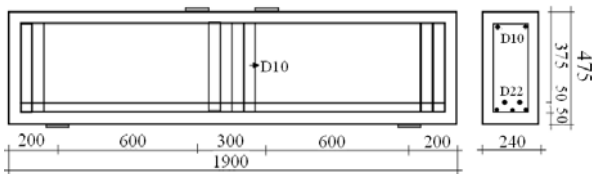| Specimen	Shear Span Ratio (a/d)	Compressive Strength (fc')
B2	0.5	36.2
B10	1.5	29.2

Figure 4. Deep beam B2 (a/d=0.5).

Figure 5. Deep beam B10 (a/d=1.5).

4 SIMULATION OF DEEP BEAM B2

4.1 *Experimental test results*

Experimental load-displacement curve of B2 deep beam is indicated by dashed line in Figure 6. Crack Propagation is shown in Figure 7.1 (Kosa et al. 2005 and 2006). It was reported that, first shear crack occur at P=525 kN (a) (shown as "a" point in Fig. 6) starting from the middle of the support plate (Fig. 7.1.a). At P=800 kN (b), diagonal crack propagate and bending crack occur at the center of the span (Fig. 7.1.b). Diagonal cracks are connected and near loading and support points, several fine cracks are formed in different direction due to compressive stress. At peak load, which is 1550 kN (c), diagonal cracks develop and finally concrete spalling occurs near loading and support plates with shear failure (Fig. 7.1.c). The crack width on the diagonal crack at peak load was given 0.25 mm.

4.2 *Comparison of analytical and experimental results*

Analytical load displacement graph is shown by solid line in Figure 6. Initial stiffness in the analysis is higher than the experimental one. However, it agreed with the theoretical one. Analytical peak load is 1722 kN (C) where it shows slightly higher value compared to the experimental one. The graphs show significant agreement in post-peak region.

Crack Propagation for numerical analysis is given in Figure 7.2. The magnification factors in the figures are 200, 100 and 40 respectively. The shear crack becomes significant at P=723 kN (Fig. 7.2.a), which is a point of the load displacement graph that the stiffness slightly changes (A). The length and direction of the crack are similar and agreed well with the experimental one. At P=1172 kN (B) (Fig. 7.2.b), which is 0.68 times of Pmax, we can observe similar behavior with experimental one shown in Figure 7.1.b. At the peak load, main shear cracks extend from inner side of the support plates and outer side of the loading plates towards to the compression struts (Fig. 7.2.c). Crack pattern are reasonably similar with the experimental result. That is, the length and directions agreed reasonably well for outer and inner diagonal cracks. Furthermore, the analytical crack width measured on the diagonal shear crack is 0.27 mm at peak load, which agreed well with the experimental one that is 0.25 mm.

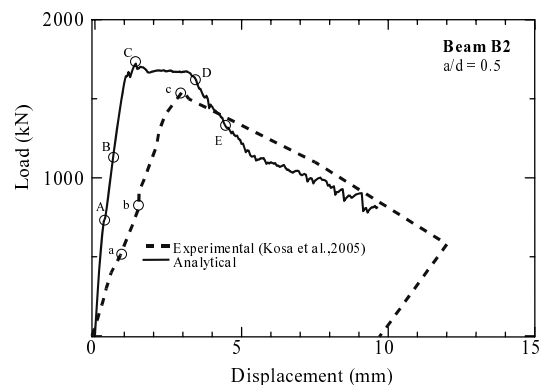As a result, the analytical results performed by RBSM show good agreement with the experimental ones as discussed.
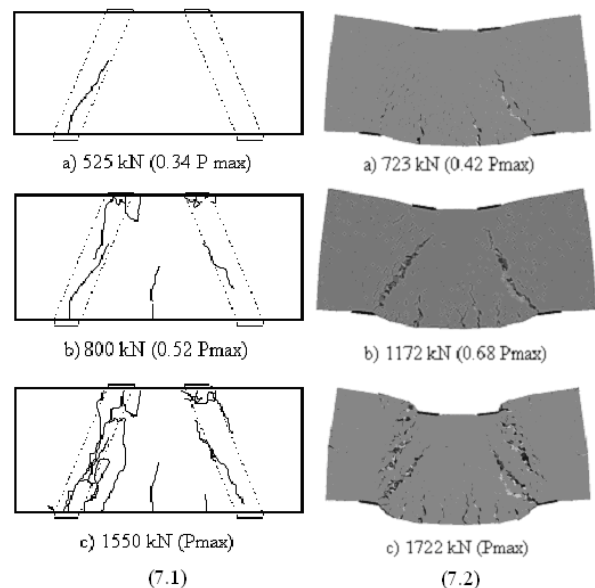
Figure 6. Load displacement graph.

Figure 7. Crack propagation 7.1) experimental, 7.2) analytical.

4.3 Deformation of the beam in post-peak region

3D-RBSM analysis provides deformation shape three dimensionally, which allows inquiring failure mechanism in detail. Figure 8 shows 3D deformed shape in peak and post-peak steps. Deformed shapes are magnified in order to observe the failure behavior clearly. The magnification factor is 40 for all cases.

a) Peak Load P=1722 kN

b) Post-Peak Load P= 1590 kN
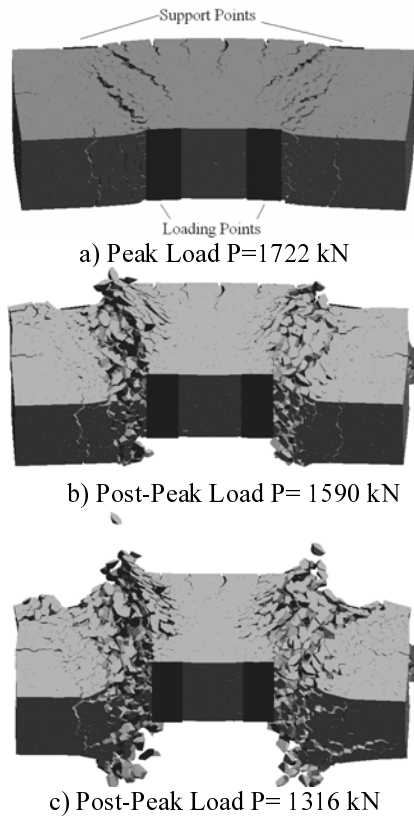
c) Post-Peak Load P= 1316 kN

Figure 8. 3D Deformed shape.

At the peak load (Fig. 8.a), spalling behavior along the strut cannot be observed. However, just after the peak load, spalling of concrete occurs along the strut. The lateral deformation increases as shown in Figure 8.b, which shows 3D deformed shape at post-peak load P=1590 kN (D). Then, flexural behavior is not observed. Figure 8.c shows 3D deformed shape at post-peak load P=1316 kN (E). Spalling of concrete and lateral deformation increase in further loading steps at post-peak that can be investigated clearly by comparing the figures.

4.4 Discussion on the compression strut

Figure 9 shows the principle stress distribution on the longitudinal middle section of the beam. Maximum stress range is set to f'c=36.2 MPa. The stress distribution at pre-peak load P=1172 kN (B) is shown in Figure 9.a. The strut initiation can be seen in the figure.

The stress distribution at peak load (C) is given in Figure 9.b in which the strut appears clearly. Figure 9.c shows the strut at post peak load P=1316 kN (E). Especially in the middle height of the beam, the strut increases significantly.

Strut widths are compared near the loading points (Point 1), support points (Point 3) and middle height of the beam (Point 2) shown in Figure 10.

a) Pre-Peak Load P= 1172 kN

b) Peak Load P= 1722 kN
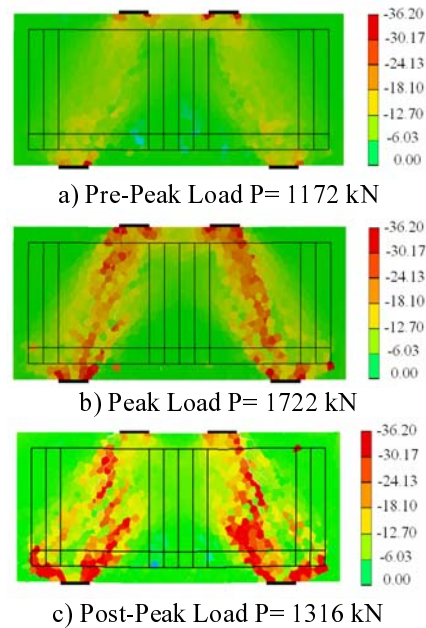
c) Post-Peak Load P= 1316 kN

Figure 9. The principle stress distribution on the longitudinal middle section.
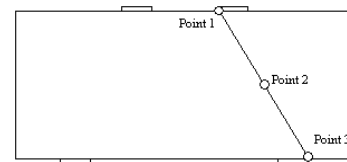
Figure 10. The strut and stress measurement points.

Figure 11 shows the comparison of normalized strut widths on point 1, point 2 and point 3 both measured for the surface and middle longitudinal section of the beam. The strut is defined by the area where the stress is over 0.5fc' and then the widths are measured and normalized by plate width. At point 2, the strut width reaches more than 2.5 times of the plate width on the surface section and it reaches 3 times of the plate width on the middle section. In the case of point 1 and 3, the width is about 1.5 times for both surface and middle section.
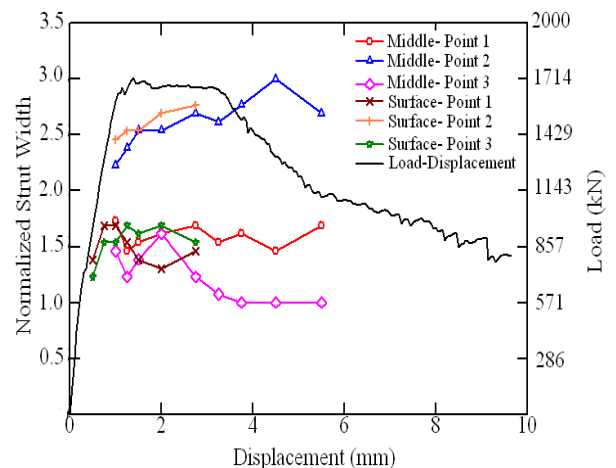
Figure 11. The comparison of strut widths.

The strut on the surface section disappears in post-peak region. On the other hand, it is observed until the post-peak load P = 1109 kN in the case of middle section. Due to the spalling of concrete on the surface of the beam, the strut disappears in early post-peak steps for surface section.

4.5 *Discussion on the change of high compressive stress*

The high complex stress state is a significant issue in deep beams. The high stress, which is greater than the compressive strength of concrete (fc'), localizes near support and loading points and within the compression strut. Stress concentration within these areas can be observed clearly in Figure 9.

Figure 12 shows the change of the normalized stress along the compression strut. The stress values are normalized by compressive strength of concrete. Three points are chosen on the strut connecting by a line shown in Figure 10. The stress is measured both on the middle and surface longitudinal section for three points separately.

As shown in the figure, the stress on all points increases similarly for both surface and middle section cases in pre-peak region. Thus, there is no 3D effect in this region.

The stress on point 1 reaches to about 2 times of fc' on surface section where it is 1.6 fc' on the middle beam section near the peak load. Then, the stress suddenly decreases on the surface. However, the stress on the middle section gradually decreases. The reason is spalling behavior on the surface, that is, the concrete cannot carry the stress after the spalling behavior occurs.

At Point 2, which is on the middle height of the beam, after the peak load, the stress on the middle section reaches to the compressive strength of concrete. Then, it continues around fc' in post-peak region. On the other hand, the stress on the surface section gradually decreases in post-peak region differing from the case of the one on the middle section.

At Point 3, which is on the support plate, the stress increase until the peak load for both cases similarly. The stress at the peak load is 45 MPa (1.24 fc') on middle section and it is 53 MPa (1.46 fc') on the surface section. However, the behavior is different in post-peak. After the peak load, the stress on the middle section proceeds to increase and finally it reaches 70 MPa (1.93 fc'). On the other hand, the stress on the surface proceeds to increase up to about 60 MPa (1.66 fc'). However, it decreases hereafter similar with the behavior of other points. Different behavior between surface and middle part appears depending on the spalling of concrete on the surface and confining effect in the middle part.

The analysis results show that three-dimensional effect is important for deep beam B2 especially for post-peak region. Therefore, 3D-RBSM is a useful tool to investigate the failure mechanism in detail since it can be simulate 3D behavior reasonably as discussed before.
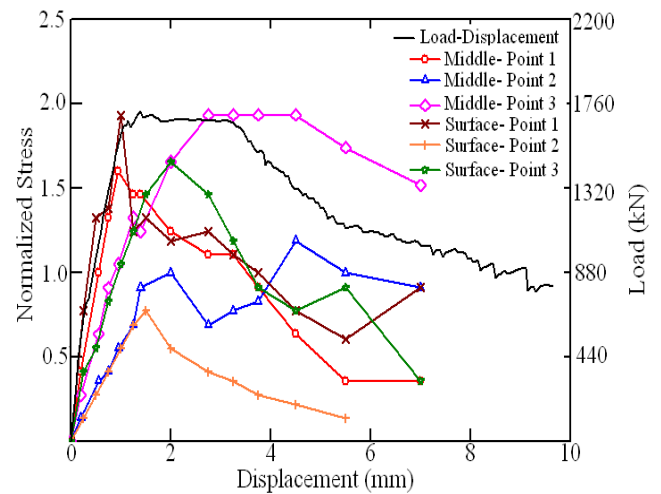

Figure 12. The change of stress.

5 SIMULATION OF DEEP BEAM B10

5.1 *Experimental test results*

Experimental load displacement curve is shown by dashed line in Figure 13. Crack propagation is given in Figure 14.1 (Kosa et al. 2005, 2006). It was reported that, the flexural cracks occur at P=225 kN (shown as "a" point in Fig. 13) in the middle part of the beam (Fig. 14.1.a). The shear cracks that occurred on support plate propagate towards to the compression strut at P=425 kN (b) (Fig. 14.1.b). Finally, the shear crack connects to the outer side of the loading plate at peak load P=616 kN (c) and then shear failure occur (Fig. 14.1.c). The crack width on the diagonal crack at peak load is given as 2.0 mm.

5.2 *Comparison of analytical and experimental results*

Analytical load displacement graph is shown by solid line in Figure 13. The peak load is 782 kN that is higher than the experimental one. The beam fails suddenly after the peak load as shown in the figure.

Analytical crack propagation is given in Figure 14.2. In order to present the crack pattern clearly, the deformed shapes magnified by 80, 40 and 20 for Figure 14.2.a, 14.2.b and 14.2.c respectively. At P=280 kN (A), flexural cracks take place in the middle span (Fig. 14.2.a) that agreed well with the experimental results (Fig. 14.1.a). After that, the first explicit shear crack is seen at near P=319 kN on lower part of the strut. Then, the cracks develop along the inside line between loading and support

plates (Fig. 14.2.b). The rapture of concrete between loading plates is observed (Fig. 14.2.c). Crack locations and directions agreed reasonably with the experimental ones.

Furthermore, the crack width on the diagonal shear crack at the peak load is measured as 2.0 mm, which is the same with the experimental one.
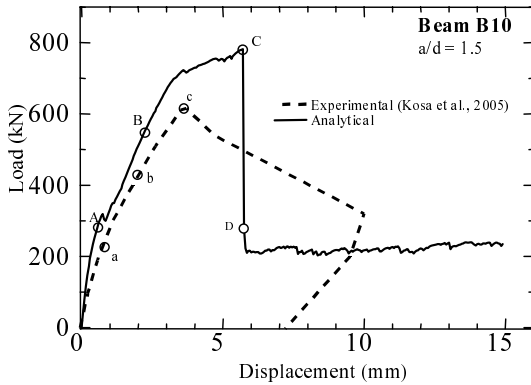

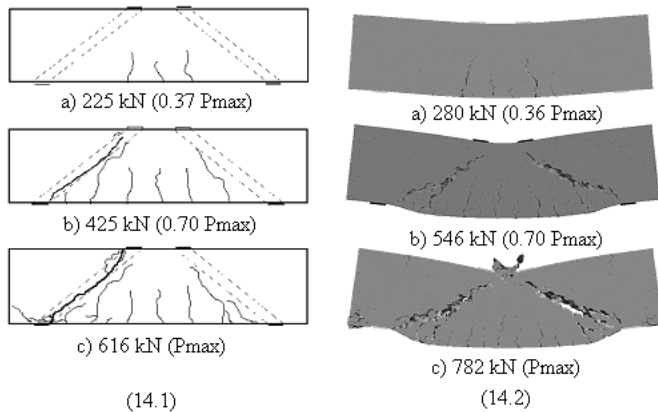Figure 13. The load displacement graph B10.

Figure 14. Crack propagation 14.1) experimental, 14.2) analytical.

5.3 Deformation of the beam in post-peak region

Figure 15 shows 3D deformed shapes of the beam at peak load P=782 kN (C) and at post-peak load P=278 kN (D). Deformed shapes are magnified in order to observe the behavior clearly. The magnification factor is 40 for all cases.
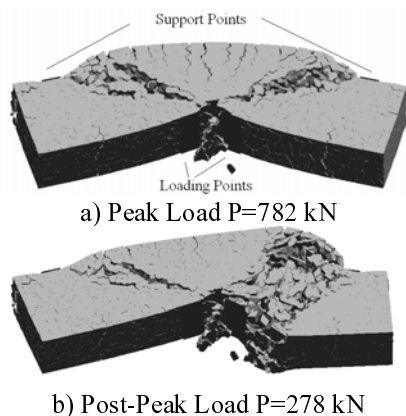

a) Peak Load P=782 kN

b) Post-Peak Load P=278 kN
Figure 15. 3D Deformed shape.

The shear failure is observed just after the peak load as seen in the figures. Spalling behavior is observed along the strut. The difference of deformation with the case of a/d=0.5 is obviously understood. That is, the lateral deformation is not dominant in this case. This can be confirmed from the behavior of compression strut in the next section.

5.4 Discussion on the compression strut

Figure 16 shows the principle stress distribution on the longitudinal middle section for different steps.

a) Pre-Peak Load P= 546 kN
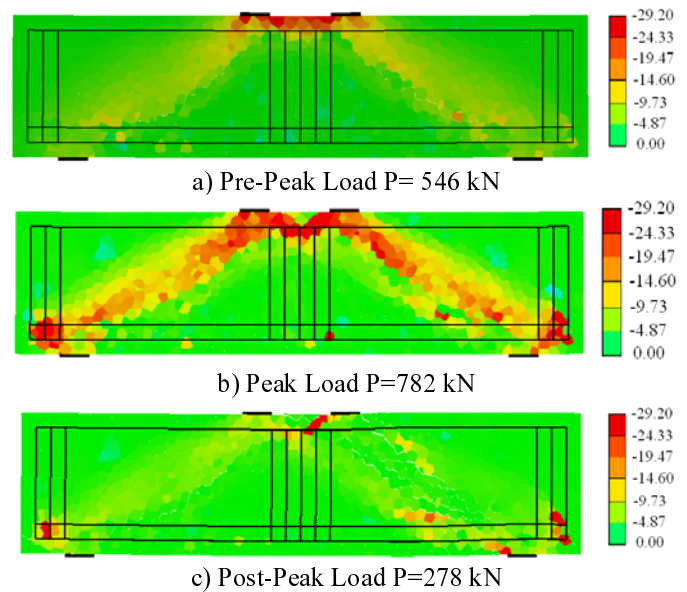

b) Peak Load P=782 kN

c) Post-Peak Load P=278 kN
Figure 16. The principle stress distribution on the longitudinal middle section.

Maximum stress range is set to f'c=29.2 MPa. The strut initiation can be seen in Figure 16.a at pre-peak load P=546 kN (B).

The stress distribution at peak load (C) is given in Figure 16.b in which the strut appears clearly. At post-peak load P=278 kN (D), the strut disappears suddenly due to sudden failure of the beam (Fig. 16.c).

Strut widths are compared near the loading points (Point 1), support points (Point 3) and middle height of the beam (Point 2) mentioned in the case of B2 (Fig. 10).

Figure 17 shows the comparison of normalized strut widths both measured for the surface and middle longitudinal section of the beam. The widths are normalized by plate width.

At point 2, which is on the middle height, the strut on the surface shows similar increase with load displacement curve until the peak load. It has slightly higher value compared to the one on the middle section in pre-peak region. The strut width reaches 2.5 times of the plate width near peak on both surface and middle section.

The strut on the loading point (Point 1) reaches to about 1.5 times of the plate width on both middle

and surface section. The width in pre-peak region has almost constant value in average. The strut on support plate (Point 3) equals about the plate width in pre-peak region and similar for both surface and middle section. The strut widths are available only in pre-peak region since the strut suddenly disappears just after the peak load.
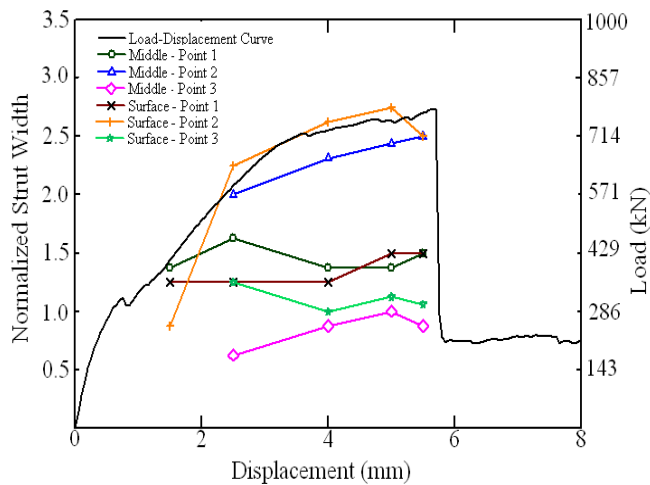

Figure 17. The comparison of strut widths.

The strut behavior is compared between B2 (a/d=0.5) and B10 (a/d=1.5). The strut widths on point 1 (loading plate) are similar in both cases, which is about 1.5 times of the plate width. The widths on point 2 (middle height) are also similar and about 2.5 times of the plate width in both B2 and B10. However; In point 3 (support plate), the strut in B2 is about 1.5 times of plate width and it is wider than the strut in the case of B10, which is equal to plate width. The reason is that, in the case of B2 (a/d=0.5), the stress flows along the strut from loading points to support points based on tied strut mechanism. Thus, the width on the support plate (Point 3) is the same with the one on the loading plate. On the other hand, both arch action and flexural behavior occur in B10 (a/d=1.5) and the stress increase between loading plates (Fig. 16.b). Therefore, the strut near the support is smaller in this case compared to the case of B2.

5.5 *Discussion on the change of high compressive Stress*

Figure 18 shows the change of the stress, which is normalized by fc'. The stress is measured on the points given in Figure 10 for both on the middle and surface longitudinal section.

Point 1 shows the change of stress on loading plate. The stress on the middle section increases parallel with the load. It reaches about 1.5fc' at peak load. Then, the high stress suddenly disappears after the peak due to sudden failure of the beam.

Point 2 shows the change of stress on the middle height of the beam. The stress increases similarly

until the peak load on both surface and middle section shown in the figure. The stress values are less than fc' for both case in pre-peak region.

Point 3 shows the change of stress on the support plate. The stress value on the middle section is higher than the surface section. The stress value is less than fc' for both case in pre-peak region.

The high stress state is compared between B2 (a/d=0.5) and B10 (a/d=1.5) and discussed. As seen in the figure, the high stress occurs only at point 1 (loading plate) and at point 3, the high stress cannot be observed due to occurrence of flexural behavior in the case of B10.

The results show that, three-dimensional behavior is not dominant in B10 (a/d=1.5) deep beam where it is important in the case of B2 (a/d=0.5).
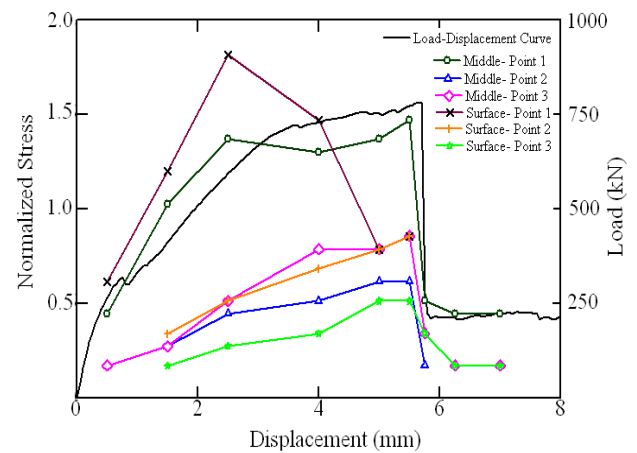

Figure 18. The change of stress.

6 CRACK GROWTH RATE DUE TO A/D

RBSM results provide useful information such as crack widths that can be measured and they can be investigated step by step. The change of crack widths is given in Figure 19 for B2 and B10 deep beams. Crack widths are measured on the diagonal shear crack. The analytical crack widths are compared in order to investigate the effect of shear span ratio (a/d) on the behavior of deep beams.
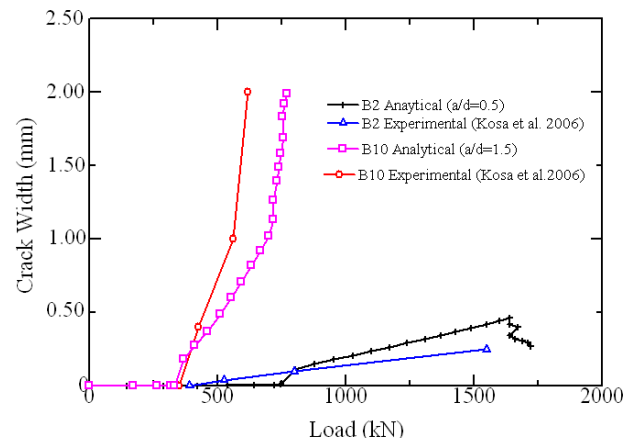

Figure 19. Change of crack widths of B2 and B10 deep beams.

As seen in the figure, the shear crack width starts to increase after P= 723-745 kN in deep beam B2. However, the growth rate is limited yet. The crack width in deep beam B10 increases starting from P= 319-367 kN. Then, it grows up rapidly as shown in the figure. The growth rate increases and the crack width reaches to 2.0 mm at the peak load.

Furthermore, the change of the crack widths in the experiments (Kosa et al. 2006) is given in Figure 19. The analytical and experimental results are agreed well. It is clear that, RBSM can simulate the cracking behavior reasonably well.

7 CONCLUSIONS

(1) Deep beams without web reinforcement and having shear span ratio of 0.5 and 1.5 are analyzed by 3D-RBSM. Analytical load displacement graphs, crack propagation and crack patterns and measured crack widths are compared with the experimental ones for B2 and B10 and it is shown that 3D-RBSM results shows reasonable agreement with the experimental results.

(2) 3D deformations in peak and post-peak region are discussed and lateral deformation is investigated in deep beams. Moreover, the strut widths and high stress state on both surface and middle longitudinal section are compared and discussed in order to investigate the 3D effect.

In deep beam B2 (a/d=0.5), the strut on the surface disappear in early post-peak loads compared to the middle one due to spalling behavior of concrete. Furthermore, different stress state is observed on surface and middle section due to spalling of concrete and confinement effect. Thus, 3D effect is important and RBSM can simulate 3D behavior reasonably.

In deep beam B10 (a/d=1.5), the strut and high stress cannot be observed due to sudden failure of the beam in the post-peak region. In pre-peak, high stress is observed only on the loading point.

The results show that, three-dimensional behavior is important in B2 (a/d=0.5) where it is not dominant for B10 (a/d=1.5).

(3) Crack growth rate obtained from the analysis and the experimental one shows good agreement. That is, RBSM can simulate cracking behavior realistically. It is also shown that the shear span ratio strongly affects the cracking behavior in deep beams.

REFERENCES

Bolander, J.E. & Hong, G.S. 2002. Rigid-Body-Spring Network Modeling of Prestressed Concrete Members. *ACI Structural Journal* 99 (5): 595-604
Bolander, J.E., Hong, G.S. & Yoshitake, K. 2000. Structural Concrete Analysis Using Rigid-Body-Spring Networks. *Computer-Aided Civil and Infrastructure Engineering* 15: 120-133
Kawai, T. 1978. New Discrete Models and Their Application to Seismic Response Analysis of Structures. *Nuclear Engineering and Design* 48: 207-229
Kosa, K., Umemoto, Y., Nishioka, T. & Kobayashi, H. 2005. Experimental Studies on Failure Mode in the Deep Beam. *Journal of Structural Engineering-JSCE* 51A: 1283-1290 (In Japanese).
Kosa, K., Wakiyama, T., Nishioka, T. & Kobayashi, H. 2006. Effect of Shear Span Ratio on the Fracture of Deep Beams. *Doboku Gakkai Ronbunshuu E* 62(4): 798-814 (In Japanese)
Saito, S. 1999. Fracture Analyses of Structural Concrete Using Spring Networks With Random Geometry. *PhD Dissertation*. Kyushu University
Yamamoto, Y., Nakamura, H., Kuroda, I. & Furuya, N. 2008. Analysis of Compression Failure of Concrete by Three Dimensional Rigid Body Spring Model. *Doboku Gakkai Ronbunshuu* 64(4): 612-630 (In Japanese)